

Retrieving intracycle interference in angular-resolved laser-assisted photoemission from argon

Johan Hummert¹, Markus Kubin^{1,2}, Sebastián D. López³, Marc J. J. Vrakking¹, Oleg Kornilov¹, and Diego G. Arbó³

¹Max-Born-Institute, Max-Born-Straße 2A, 12489 Berlin, Germany

²Institute for Methods and Instrumentation for Synchrotron Radiation Research, Helmholtz-Zentrum Berlin für Materialien und Energie GmbH, Albert-Einstein-Strasse 15, 12489 Berlin, Germany

³Institute for Astronomy and Space Physics IAFE (CONICET-UBA) CC 67, Suc. 28, C1428ZAA, Buenos Aires, Argentina

Received: date / Revised version: date

Abstract. We report on a combined experimental and theoretical study of XUV ionization of atomic argon in the presence of a near-infrared laser field. The resulting energy- and angle- resolved photoemission spectra have been described in the literature as interferences among different photoionization trajectories. Electron trajectories stemming from different optical laser cycles give rise to *intercycle* interference energy and result in new peaks known as sidebands. These sidebands are modulated by a coarse grained (gross) structure coming from the *intracycle* interference of the electron trajectories born during the same optical cycle. We calculate the photoelectron emission by solving the time-dependent Schrödinger equation *ab initio* and within the continuum-distorted wave strong field approximation. In order to compare with the experimental data we average the calculated energy-angle probability distributions over the experimental focal volume. This averaging procedure washes out the intracycle interference pattern, which we experimentally and theoretically (numerically) recover by subtracting two averaged distributions for slightly different near-infrared laser field intensities.

PACS. 32.80.Fb Photoionization of atoms and ions – 32.80.Wr Other multiphoton processes – 03.65.Sq Semiclassical theories and applications

1 Introduction

Generation of XUV pulses via high order harmonics opens new routes for time-resolved spectroscopy with unprecedented time resolution. In combination with near-infrared or visible (NIR/vis) laser light such XUV pulses allow for control of electron motion on ultrashort timescales. The most readily observed effect in such experiments is the laser-assisted photoelectric effect (LAPE), where the NIR/vis light controls trajectories of free electrons created by the short XUV pulses. For XUV pulses longer than the control laser cycle T_L , the photoelectron energy spectrum shows a main line associated with the absorption of one XUV photon accompanied by sideband (SB) lines. The equally spaced SBs with separation $\hbar\omega_L$ are associated with additional exchange of few NIR photons through absorption and stimulated emission processes. The sidebands have been observed in laser-assisted ionization of gases, liquids and solids and can be used to extract information on the XUV pulse duration, control laser intensity, and time delay between the two pulses [1, 2, 3, 4].

For sufficiently high intensity of the control NIR/vis pulse another class of features appears in photoemission spectra, which stem from the intracycle interferences. For linearly polarized pulses they are manifested in modula-

tions of photoelectron angular distributions. This effect has been established for ionization of Ne and other noble gases at free-electron laser facilities (FEL) and compared with calculations [5, 6, 7]. However, to the best of our knowledge, a detailed analysis of features in angular- and energy-resolved photoelectron spectra has not been performed. We fill this gap and present a combined experimental and theoretical study of intracycle and intercycle interferences in LAPE from Ar atoms.

An accurate theoretical description of the LAPE process must be based on quantum mechanical concepts, i.e., on *ab initio* solutions of the time dependent Schrödinger equation (TDSE) for the atomic system in the presence of the electric field of two laser pulses. However, the precise calculation of the response of a rare gas atom presents considerable difficulties. Often, the numerical solution of the TDSE is employed, which relies on the single-active-electron (SAE) approximation, with model potentials that permit one to reproduce the bound state spectrum of the multi-electron atom with a satisfactory accuracy [8, 9]. Models based on a time-dependent distorted wave theory, like the strong field approximation (SFA) and the Coulomb-Volkov approximation (CVA), have also been extensively employed to study LAPE (see for example [10, 11, 12]). To gain physical insight it is often useful to com-

pare full numerical results with qualitative predictions. For example, the simple man’s model [13] has been very useful for the case of above-threshold ionization (ATI) by one-color lasers where it is possible to describe the photoelectron spectra as the interplay of intra- and intercycle interferences of electrons’ trajectories [14, 15]. On equal footing, the photoelectron spectra of LAPE has recently been treated as an interference problem in the time domain [16, 17, 18]. Electron trajectories stemming from different optical laser cycles give rise to *intercycle* interference, which results in new peaks, known as sidebands, modulated by a coarse-grained structure coming from the *intracycle* interference of the electron trajectories born during the same optical cycle [16, 17, 18].

In this paper, a detailed experimental and theoretical study of energy and angle-resolved sideband spectra are presented. XUV pulses from HHG are filtered by a time-delay-compensating monochromator [19] and combined with the fundamental femtosecond NIR pulses. Owing to precise synchronization of the laser pulses this experimental scheme does not suffer from time jitter experienced in FEL-based experiments [4]. The small bandwidth of the XUV pulses from the monochromator can be used to study photoelectron sidebands which are free from interference effects from adjacent harmonic orders. This setup is hence an ideal tool for the investigation of sideband generation and the related physics of strong-field and multiphoton nonlinear effects which occur in LAPE. In combination with the velocity map imaging spectrometer [20], angular distributions can be measured, which render additional information on the photoionization process, such as the partial wave character of the emitted photoelectrons or relative ionization phases.

We also perform theoretical calculations solving the full TDSE *ab initio* and employing the SFA to reproduce the experimental measurements. We analyze angle-resolved photoelectron distributions of atomic argon in the case where the duration of the XUV pulse τ_X is of the order of or larger than the laser cycle period, i.e., $\tau_X \gtrsim T_L$. The role of the NIR laser field in the XUV photoionization is threefold: (a) due to Stark effect, it shifts the energy of the continuum states of the atom down by the ponderomotive energy U_p , (b) several NIR photons can be absorbed or emitted in the course of the ionization process giving rise to SBs (or intercycle contributions), and (c) it is responsible for intracycle modulations of the SBs in the photoelectron angle-resolved spectrum. For the latter, the interfering electron trajectories within the same optical cycle give rise to a well-determined modulation pattern encoding information of the ionization process in the sub-femtosecond time scale. A similar behavior has been observed by J-W. Geng *et al.* in [21] for single ionization of He by considering two XUV attosecond pulses separated by the duration of the laser cycle period. In the experiments the intensity of the NIR field varies across the laser focus leading to “washing out” of the interference features, which are very sensitive to the field strength [22]. To compare theoretical calculations with the experimental results

we implement averaging of the calculated spectra over the focal volume.

The paper is organized as follows. In Sec. 2 we describe the two different methods of calculating angle-resolved photoelectron spectra for the case of laser assisted XUV ionization: by solving the TDSE *ab initio* and by making use of the SFA. We also describe the calculation method to simulate the averaging over the focal volume. In Sec. 3 we describe the experimental setup to measure the velocity-map images of atomic argon ionized by XUV pulses in presence of the fundamental NIR laser pulse and present the experimental results. In Sec. 4, we present the theoretical results obtained solving the TDSE and within the SFA, compare them with the measurements, and discuss the details of the sideband gross structure. Concluding remarks are presented in Sec. 5.

2 Methods of calculation

We solve the problem of atomic ionization by an XUV pulse in the presence of an NIR laser field with both fields linearly polarized along the \hat{z} direction. We use atomic units in this section, except when otherwise stated. The TDSE in the single active electron approximation reads

$$i\frac{\partial}{\partial t}|\psi(t)\rangle = H|\psi(t)\rangle, \quad (1)$$

where the Hamiltonian of the system within the dipole approximation in the length gauge is expressed as

$$H = \frac{\mathbf{p}^2}{2} + V(r) + \mathbf{r} \cdot \mathbf{F}_X(t) + \mathbf{r} \cdot \mathbf{F}_L(t). \quad (2)$$

The first term in Eq. (2) corresponds to the active electron kinetic energy, the second term is the potential energy of the active electron due to the Coulomb interaction with the core, and the last two terms correspond to the interaction of the atom with the electric fields of the XUV pulse $\mathbf{F}_X(t)$ and the NIR pulse $\mathbf{F}_L(t)$.

As a consequence of the interaction between the atom and the XUV and NIR pulses, the bound electron in the initial atomic state $|\phi_i\rangle$ is emitted into the final unperturbed state $|\phi_f\rangle$ with energy $E = k^2/2$ and angle θ with respect to the polarization axis \hat{z} . The angle- and energy-resolved continuum photoelectron distribution can be calculated as

$$\frac{dP}{\sin\theta dEd\theta} = 2\pi\sqrt{2E}|T_{if}|^2, \quad (3)$$

where T_{if} is the T-matrix element corresponding to the transition $\phi_i \rightarrow \phi_f$. Eq. (3) uses the cylindrical symmetry of the problem around the polarization axis.

2.1 Time-Dependent Schrödinger Equation

We employ the generalized pseudo-spectral method to numerically solve the TDSE in the length gauge of the dipole approximation in the SAE approximation [23, 24, 25]. Within

this method the discretization of the radial coordinate is optimized to incorporate the Coulomb singularity. Additionally suitable quadrature methods allow for a stable long-time evolution using a split-operator representation of the time-evolution operator. Both bound as well as unbound parts of the wave function $|\psi(t)\rangle$ can be accurately represented. The atomic potential $V(r)$ is modelled as the sum of the asymptotic Coulomb potential, $V(r) = -1/r$, and a short-range potential accounting for the influence of the ionic core of Ar^+ . Its parameters are chosen to reproduce the ionization potential $I_p = 15.76$ eV and the energies of lower excited bound states [26]. Propagation of the wavefunction starts from the initial $3p$ ground state orbitals φ_{3p0} since the ionization from the $m = 0$ orbital, aligned along the laser polarization axis, strongly dominates over $m = -1, 1$ in the resulting spectrum. Due to the cylindrical symmetry in a linearly polarized laser field, the magnetic quantum number is conserved during the time evolution. After integrating over the duration of the pulse, the wavefunction is projected onto eigenstates $|k, \ell\rangle$ of the field-free atomic Hamiltonian with positive eigenenergy $E = k^2/2$ and orbital quantum number ℓ to determine the transition amplitudes T_{if} (see Refs. [27, 28, 29]), i.e.,

$$T_{if} = \frac{1}{\sqrt{4\pi k}} \sum_{\ell} e^{i\delta_{\ell}(p)} \sqrt{2\ell+1} P_{\ell}(\cos\theta) \langle p, \ell | \psi(t_f) \rangle. \quad (4)$$

In Eq. (4), $\delta_{\ell}(p)$ is the momentum-dependent atomic phase shift, θ is the angle between the electron momentum \mathbf{k} and the polarization direction \hat{z} , and P_{ℓ} is the Legendre polynomial of degree ℓ . In order to minimize unphysical reflections of the wave function at the boundary of the calculation box, the length of the calculation box was chosen to be 1200 a.u. (~ 65 nm) and the maximum angular momentum considered was $\ell_{\max} = 300$.

2.2 Strong field approximation

Within the time-dependent distorted wave theory, the transition amplitude in the post form and length gauge is expressed as

$$T_{if} = -i \int_{-\infty}^{+\infty} dt \langle \chi_f^-(\mathbf{r}, t) | [\mathbf{r} \cdot \mathbf{F}_X(t) + \mathbf{r} \cdot \mathbf{F}_L(t)] | \phi_i(\mathbf{r}, t) \rangle \quad (5)$$

where $\phi_i(\mathbf{r}, t) = \varphi_i(\mathbf{r}) e^{iI_p t}$ is the initial atomic state with ionization potential I_p and $\chi_f^-(\mathbf{r}, t)$ is the distorted final state [30]. As the SFA neglects the Coulomb distortion in the final channel, the distorted final wave function can be written as $\chi_f^-(\mathbf{r}, t) = \chi^V(\mathbf{r}, t)$, where

$$\chi^V(\mathbf{r}, t) = \frac{\exp[i(\mathbf{k} + \mathbf{A}(t)) \cdot \mathbf{r}]}{(2\pi)^{3/2}} \exp\left[\frac{i}{2} \int_t^{\infty} dt' (\mathbf{k} + \mathbf{A}(t'))^2\right] \quad (6)$$

is the length-gauge Volkov state [31] and $\mathbf{A}(t) = -\int_{-\infty}^t \mathbf{F}(t') dt'$ is the vector potential due to the combined electric field

$$\mathbf{F}(t) = \mathbf{F}_L(t) + \mathbf{F}_X(t). \quad (7)$$

For the sake of simplicity, we consider ionization of atomic argon which we model as a hydrogen-like atom with effective charge $Z_{eff} = \sqrt{2n^2 I_p}$, where n is the principal quantum number of the initial state. This effective charge ensures the ionization potential to be taken into account properly and, consequently, the intra- and inter-cycle fringes in electron spectra to be situated at the correct energy values compared to full TDSE simulations. For electron energies far away from the ionization threshold, the SFA is well known to give a good description of LAPE. The good agreement between SFA and TDSE ionization simulations in LAPE arises from the fact that the main contribution to the ionization comes from on-shell transitions, contrarily to NIR ionization, where off-shell transitions are dominant. In other words, the absorption and emission of photons in LAPE take place over real states: Firstly, an energetic XUV photon is absorbed followed by the absorption and emission of NIR laser photons into the continuum.

2.3 Average over the focal volume

Laser intensity variation over the focal volume implies variations of the LAPE spectra. Following the work of Posthumus for a single color laser [32, 33], we characterize the intensity profile by a Lorentzian distribution along the laser propagation direction $\hat{\zeta}$ and a Gaussian distribution along the radial direction $\hat{\rho}$ in the perpendicular plane, with cylindrical symmetry around the ζ axis. In the center of the waist (where the focusing effect is maximum), i.e., at $\zeta = \rho = 0$, the intensity of the XUV and laser fields are I_{X0} and I_{L0} , respectively. Within these assumptions, the intensity distribution for the XUV and NIR laser beams are

$$I_{X,L} = \frac{I_{X0,L0}}{1 + \left(\frac{\zeta}{\zeta_{X,L}}\right)^2} \exp\left\{-\frac{2\rho^2}{w_{X,L}^2 \left[1 + \left(\frac{\zeta}{\zeta_{X,L}}\right)^2\right]}\right\}, \quad (8)$$

where $w_{X,L}$ is the waist radius, and $\zeta_{X,L}$ is the Rayleigh range of the corresponding XUV (X) and NIR laser (L) beams. The Rayleigh length $\zeta_{X,L}$ can be calculated as

$$\zeta_{X,L} = \frac{w_{X,L}^2 \omega_{X,L}}{2c}, \quad (9)$$

and is proportional to the frequency $\omega_{X,L}$, where c is the speed of light. The volume where ionization takes place is limited to the region of overlap of the argon jet and the laser beam, which we suppose to be symmetric at the waist, i.e., $-\zeta_{\text{jet}} \leq \zeta \leq \zeta_{\text{jet}}$.

The average over the focal volume of the angle-resolved photoelectron spectrum is defined as

$$\left\langle \frac{dP}{\sin\theta dE d\theta} \right\rangle = \frac{1}{V} \int \left(\frac{dP}{\sin\theta dE d\theta} \right) dV, \quad (10)$$

where the $dP/(\sin\theta dEd\theta)$ is the electron emission distribution calculated for the XUV and NIR intensities I_X and I_L , respectively. Considering the focal volume described above, Eq. (10) becomes

$$\left\langle \frac{dP}{\sin\theta dEd\theta} \right\rangle = \frac{2\pi}{V} \int_0^\infty d\rho \rho \int_{-\zeta_{\text{jet}}}^{+\zeta_{\text{jet}}} d\zeta \left(\frac{dP}{\sin\theta dEd\theta} \right). \quad (11)$$

In order to calculate the average of Eq. (11), we must integrate over the variables ρ and ζ or, equivalently, over the variables I_X and I_L through Eq. (8). As the calculations of $dP/(\sin\theta dEd\theta)$ for a single intensity are a challenge by themselves, performing the average of Eq. (11) becomes computationally very expensive. For example, if we choose a grid of n points per each I_X and I_L intensity, we would need n^2 calculations of the distribution for the n^2 pairs of intensities (I_X, I_L) . In the following we show how to overcome this difficulty with a valid physical criterion.

From TDSE and SFA calculations we have observed that for moderate laser intensities the contribution to ionization due to the XUV and NIR laser pulses are well separated in the energy domain: Whereas the single-photon XUV ionization leads to ionization with final kinetic energy close to $E \simeq \omega_X - I_p$, ionization due to the NIR pulse only [setting $\mathbf{F}_X = 0$ in Eq. (2) and Eq. (5)] leads to electrons with final kinetic energy less than twice the ponderomotive energy $E \lesssim 2U_p$. If we focus on the emission due to the XUV pulse around $E \simeq \omega_X - I_p$, the contribution from NIR ionization is negligible provided $U_p \ll \omega_X - I_p$. With this in mind and considering the first Born approximation for ionization by one XUV photon, the ionization probability is proportional to the intensity of the XUV field, i.e., $P \propto I_X$ in the ionization zone $-\zeta_{\text{jet}} \leq \zeta \leq \zeta_{\text{jet}}$. Moreover, the NIR laser field affects the overall structure of the photoelectron distribution with essentially no effect on the total ionization yield, hence, we can say to a good degree of approximation that

$$\left. \frac{dP}{\sin\theta dEd\theta} \right|_{I_X, I_L} = \left(\frac{I_X}{I_{X0}} \right) \left. \frac{dP}{\sin\theta dEd\theta} \right|_{I_{X0}, I_L}. \quad (12)$$

We have tested that Eq. (12) is correct to a high level of accuracy with TDSE and SFA calculations. Since the evaluation for one single value of I_{X0} is enough to calculate the same for a different value I_X through Eq. (12), a grid in the XUV intensity is not needed. Therefore, instead of n^2 values of the distribution [for the $n \times n$ values of (I_X, I_L)], we need only n different values of the distribution for the n different values of I_L .

3 Experimental setup and results

The experiments are carried out at the XUV time-delay-compensating monochromator beamline described in detail elsewhere [19, 34]. In short, 1.5 mJ pulses from a Ti:Sapp laser system with durations of 25 fs and repetition rate of 1 kHz are used to generate high-order harmonics in Ar. The XUV spectrum consists of a sequence of odd harmonics of the driving laser field (800 nm) spanning the photon

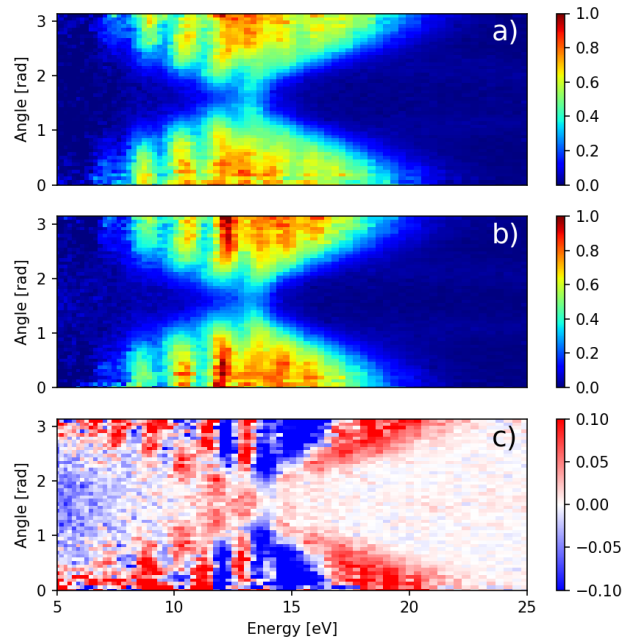


Fig. 1. Reconstructed energy-angle distributions of laser-assisted photoemission spectra. The argon atoms are ionized by 29.6 eV XUV photons (harmonic 19) in the presence of the 800 nm laser field with the intensities of a) 14 TW/cm², b) 13 TW/cm². In (c) the difference map for the two measurements of (a) and (b) is presented. Red colors indicate the signal enhancement in the velocity map image taken at higher laser field intensity, while blue colors indicated the depletion.

energy range from 10 to 50 eV, approximately. The XUV beam is guided through the time-delay-compensating monochromator and one harmonic is selected. Thanks to the compensation scheme the XUV pulse is not stretched by diffraction off the monochromator gratings, but remains short with the duration close to that of the driving pulse. The wavelength-selected XUV pulses are combined with the 800 nm NIR pulses using an annular mirror and are focused into the interaction region of the velocity map imaging spectrometer (VMIS), which is capable of recording energy- and angle-resolved spectra of photoemission from atoms and molecules.

The LAPE images are recorded using the 29.6 eV photons (harmonic 19) and two different NIR field intensities determined by comparing the measured spectra with the theoretical results of the next section. VMIS records an Abel projection of the 3D photoelectron distributions. The 3D distributions are recovered by Abel inversion of the raw experimental images using the BASEX reconstruction algorithm. Fig. 1 (a) and (b) shows the reconstructed 2D slices through the full 3D photoelectron distributions as false color energy-angle maps. Both maps show sets of vertical lines corresponding to the main photoemission line (XUV-only) and a set of sidebands with lower and higher kinetic energies.

Although many sidebands can be observed in these experiments, even at the high intensity of 14 TW/cm² no

modulations of the angular distributions (gross structure) are visible in the images, although estimations predict that at these laser fields the intracycle interference should play a role. From a preliminary study, we found first evidence that the absence of the gross structure in these measurements is due to the averaging over a range of NIR intensities in the focal volume [22]. In the present study, this finding is confirmed with calculated spectra, averaged over different NIR intensities. In the interaction zone of the VMIS both XUV and NIR beams have comparable focus sizes. The waist radii are very difficult to determine, which leads to uncertain XUV and IR laser intensities. Comparison to theoretical calculations in the next section are compatible with intensities of about 14 TW/cm^2 , which corresponds to waist radii of about $100 \mu\text{m}$. This is an efficient configuration for many pump-probe experiments, but in the present case it results in ionization of Ar atoms taking place at a range of NIR laser field intensities varying from the maximum to almost zero across the focal volume. Since positions of the angular features induced by intracycle interferences are expected to depend on the intensity of the NIR field, the averaging over the experimental focus washes out these structures.

To recover the gross structure we subtract the distribution recorded in Fig. 1 (b) from the corresponding of Fig. 1 (a), which are taken at slightly different NIR field intensities. The result of this subtraction is shown in Fig. 1 (c) as a false-color map. Subtracting one image from the other leaves predominantly contributions due to higher peak laser intensity in Fig. 1 (a) and thus reveals modulations in the emission angle corresponding to the intracycle interferences. This method appears to be very practical for observing gross structures in laser-assisted photoemission in the common case of matched foci of pump-probe XUV-NIR beams.

4 Theoretical results and discussion

We now turn to calculating LAPE spectra for the laser field parameters used in the experiment. To compare the different methods of calculation, TDSE and SFA, described in Sec. 2 to experimental measurements of Sec. 3, we consider a flattop envelope for the IR laser pulse which is simple to model in the calculations (this assumption has no significant influence on the results). In this sense, the NIR laser field can be written as

$$\mathbf{F}_L(t) = F_{L0}(t) \cos\left[\omega_L\left(t - \frac{\tau_L}{2}\right)\right] \hat{z}, \quad (13)$$

where the envelope is given by

$$F_{L0}(t) = F_{L0} \begin{cases} \frac{\omega_L t}{2\pi} & \text{if } 0 \leq t \leq \frac{2\pi}{\omega_L} \\ 1 & \text{if } \frac{2\pi}{\omega_L} \leq t \leq \tau_L - \frac{2\pi}{\omega_L} \\ \frac{(\tau_L - t)\omega_L}{2\pi} & \text{if } \tau_L - \frac{2\pi}{\omega_L} \leq t \leq \tau_L \end{cases} \quad (14)$$

and zero otherwise. We define the XUV pulse as

$$\mathbf{F}_X(t) = F_{X0} \sin^2\left[\frac{\pi}{\tau_X}\left(t - \frac{\tau_L - \tau_X}{2}\right)\right] \cos\left[\omega_X\left(t - \frac{\tau_L}{2}\right)\right] \quad (15)$$

for $(\tau_L - \tau_X)/2 \leq t \leq (\tau_L + \tau_X)/2$ and zero otherwise. It is well known that XUV pulse shapes play a minor role in LAPE, especially for long NIR pulses [4, 5, 6]. Therefore, we use a smooth \sin^2 -envelope centered in the middle of the NIR pulse. We consider that there is an integer number of optical cycles in the XUV pulse, i.e., $N = \tau_X/2\pi\omega_X$. The definitions of the NIR and XUV pulses in equations (13) and (14) assure a flattop vector potential $A(t)$ fulfilling the boundary conditions $A(0) = A(\tau_L) = 0$. In our calculations pulse durations are defined as total widths, i.e., $\tau_{X,L}$, and not as FWHM. We perform TDSE and SFA calculations for argon initially in a $3p$ state ($I_p \simeq 0.58 = 15.8 \text{ eV}$) ionized by an XUV pulse of frequency $\omega_X = 1.0925$ (29.73 eV), duration $\tau_X = 5T_L = 5 \times (2\pi/\omega_L) = 546.4$ (13.22 fs) and an NIR laser pulse of frequency $\omega_L = 0.0575$ (1.56 eV), duration $\tau_L = 7T_L = 764.9$ (18.5 fs). The angle- and energy-resolved electron distributions calculated via TDSE are shown in Fig. 2 (a) for peak fields $F_{L0} = 0.02$ ($I_L = 1.4 \times 10^{13} \text{ W/cm}^2$). Due to linear dependence of the electron yield on the XUV pulse intensity, we have arbitrarily chosen $F_{X0} = 0.01$ ($I = 3.5 \times 10^{12} \text{ W/cm}^2$). The respective TDSE and SFA energy-angle distributions in Fig. 2 (a) and (b) extend a bit beyond the classical boundaries drawn as dashed lines [18] due to the quantum nature of the final wave function. We observe that the electron emission is more probable along the polarization axis, i.e. at $\theta = 0^\circ$ and 180° . According to Ref. [16], the electron distribution for emission parallel to the polarization axis is classically bounded, i.e.,

$$\frac{(v_0 - F_{L0}/\omega_L)^2}{2} < E < \frac{(v_0 + F_{L0}/\omega_L)^2}{2}, \quad (16)$$

where $v_0^2/2 = \omega_X - I_p$ corresponds to the electron kinetic energy for ionization by an XUV pulse only. For argon ionization by the electric fields with the laser parameters described above the energy domain along the polarization axis must be classically bounded to 0.22 (6 eV) $< E < 0.92$ (25.1 eV), where $v_0^2/2 = 0.51 = 13.9 \text{ eV}$. According to Ref. [17], in the perpendicular direction the electron kinetic energy is classically restricted to

$$\frac{[v_0^2 - (F_{L0}/\omega_L)^2]}{2} < E < \frac{v_0^2/2}{2}, \quad (17)$$

which corresponds to 0.45 (12.3 eV) $< E < 0.51$ (13.9 eV).

The vertical iso-energy stripes in Fig. 2 (a) corresponds to the sidebands arising from the absorption of one XUV photon followed by the absorption/emission of n NIR photons in agreement with the conservation of energy equation

$$E_n = n\omega_L + \omega_X - I_p - U_p. \quad (18)$$

It is worth noticing that the energy of the XUV mainline together with all SBs are slightly shifted down by the ponderomotive energy of the NIR laser $U_p = (F_{L0}/2\omega_L)^2 = 0.03$ (0.8 eV). For perpendicular emission ($\theta = 90^\circ$), the given sidebands are missing due to the selection rule for angular momentum in agreement with theoretical predictions [17]. We can also observe in Fig. 2 (a) that the

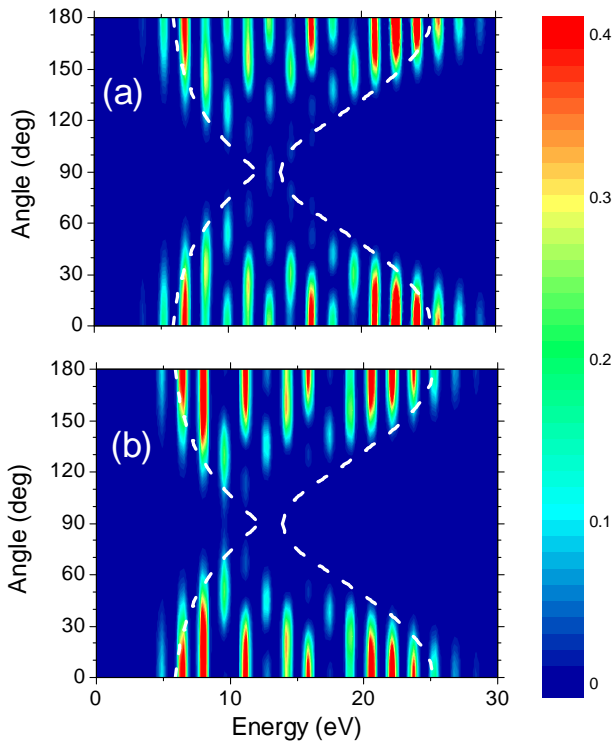


Fig. 2. Angle-energy probability distribution from Ar subject to an XUV pulse of $\omega_X = 1.0925$ (29.7 eV), duration $\tau_X = 5T_L = 5 \times (2\pi/\omega_L) = 546.4$ (13.22 fs) and a laser pulse of frequency $\omega_L = 0.0575$ (1.56 eV), duration $\tau_L = 7T_L = 764.9$ (18.5 fs). The laser peak field is $F_{L0} = 0.02$ ($I_L = 1.4 \times 10^{13}$ W/cm²) and the XUV peak field is $F_{X0} = 0.01$ ($I_X = 3.5 \times 10^{12}$ W/cm²). (a) corresponds to TDSE calculations and (b) to SFA calculations. Classical boundaries [18] are delimited by dashed lines.

sidebands are modulated by angle- and energy-dependent stripes whose origin stem from the interference of electron emission within the same optical cycle, i.e., the intracycle interference pattern (see [16, 17, 18]). In Fig. 2 (b) we show the energy-angle distribution calculated within the SFA. The resemblance to the TDSE distribution of Fig. 2 (a) is outstanding, which tells us about the minor role of the Coulomb potential in the photoionization process [15].

The SBs in Fig. 2 are modulated by a gross structure which depends on both energy and angle. In order to prove that this structure stems from the intracycle interference of electron trajectories released within the same optical laser cycle, we have performed a calculations for an XUV pulse duration of one optical cycle, i.e., $\tau_X = T_L = (2\pi/\omega_L) = 109.3$ (2.64 fs) considering a flat-top envelope instead of the \sin^2 envelope in Eq. (15). In Fig. 3 we observe that as ionization takes place essentially within the only one cycle of the NIR field, no SBs are formed, and only the intracycle interference structures remain visible in the maps. When we compare Fig. 3 with Fig. 2, we observe that the modulating stripes for the five-cycle XUV pulse in Fig. 2 look essentially the same as the

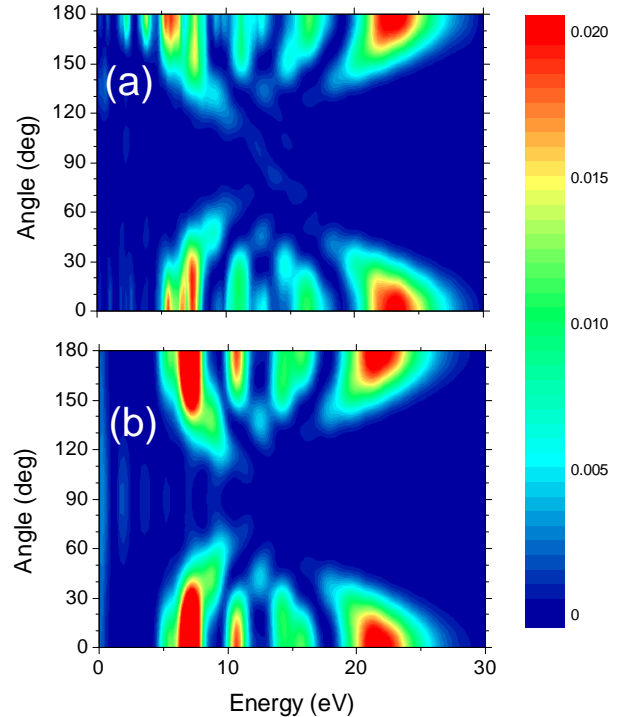


Fig. 3. Angle-energy probability distribution from Ar subject to flat-top XUV pulse of $\omega_X = 1.0925$ (29.73 eV), duration $\tau_X = T_L = (2\pi/\omega_L) = 109.3$ (2.64 fs) and a laser pulse of frequency $\omega_L = 0.0575$ (1.56 eV) and duration $\tau_L = 7T_L = 764.9$ (18.5 fs). The laser peak field is $F_{L0} = 0.02$ ($I_L = 1.4 \times 10^{13}$ W/cm²) and the XUV peak field is $F_{X0} = 0.01$ ($I_X = 3.5 \times 10^{12}$ W/cm²). (a) corresponds to TDSE calculations and (b) to SFA calculations.

intracycle structure for the $\tau_X = T_L$ calculation in Fig. 3. Again, SFA calculations in Fig. 3 (b) are in good agreement with TDSE calculations in Fig. 3 (a).

As discussed in Sec. 3, if we want to compare our simulations with the experiment, we need to average the electron spectra over the experimental intensity distribution in the focal volume (see Sec. 2.3). We assume a Gaussian profile of the NIR laser beam with a waist radius of $w_L = 0.1$ mm corresponding to a Rayleigh length of $\zeta_L = 10$ mm and also a Gaussian profile for the XUV beam with the same radius $w_X = w_L$ and corresponding Rayleigh length $\zeta_X = 190$ mm [see Eq. (9)]. We suppose an atomic beam with aperture $2\zeta_{\text{jet}} = 10$ mm. To reduce computation time, averaging is done by performing calculations for twenty values of pairs $(I_{X,i}, I_{L,i})$ with a constant ratio $I_{X,i}/I_{L,i}$ and then extrapolating for different values of I_X , according to Eq. (12). In Figs. 4 (a) and (b) we see the result of the averaging over the focal volume of the respective TDSE and SFA calculated distributions according to Eq. (11) for an XUV peak field in the focus of $F_{X0} = 0.01$ corresponding to an intensity $I_X = 3.5 \times 10^{12}$ W/cm² and a NIR laser peak field in the focus of $F_{L0} = 0.02$ corresponding to an intensity $I_L = 1.4 \times 10^{13}$ W/cm², the laser and XUV frequen-

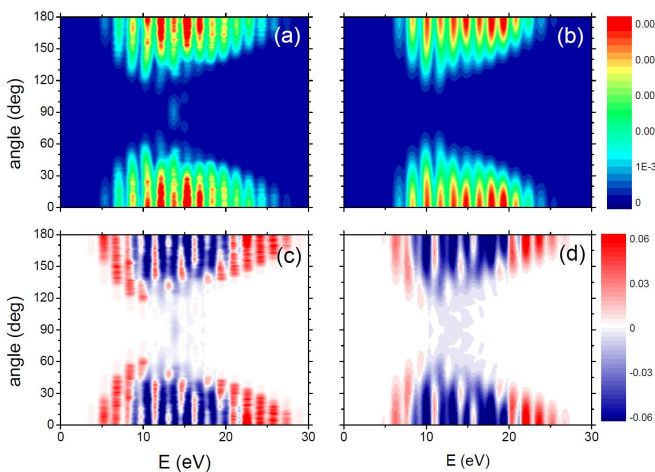


Fig. 4. Angle-energy probability distribution from Ar(3p) subject to an XUV pulse of peak field is $F_{X0} = 0.01$ ($I_X = 3.5 \times 10^{12}$ W/cm²), $\omega_X = 1.0925$ (29.73 eV), duration $\tau_X = 5T_L = 5 \times (2\pi/\omega_L) = 546.4$ (13.22 fs) and a laser pulse of frequency $\omega_L = 0.0575$ (1.56 eV), duration $\tau_L = 7T_L = 764.9$ (18.5 fs), and laser peak field $F_{L0} = 0.04$ ($I_L = 5.6 \times 10^{13}$ W/cm²). (a) and (b) distributions are averaged over the focal volume [Eq. (11)], (c) and (d) corresponds to the difference between the distributions calculated in (a) and (b) and the ones in with $F_{X0} = 0.0095$ ($I_X = 3.2 \times 10^{12}$ W/cm²) and $F_{L0} = 0.019$ ($I_L = 1.27 \times 10^{13}$ W/cm²). (a) and (c) corresponds to TDSE calculations and (b) and (d) to SFA calculations. Calculations were smoothed using an energy window of about 1 eV and an angle of about 5°.

cies and durations are the same as in Fig. 2. We observe that the general features of the distribution are similar to the non-averaged distributions in Fig. 2 (a) except for the smoothing and disappearing of the intracycle interference pattern. This lack of intracycle interference pattern agrees with the experimental observations [see Fig. 1 (a) and (b)]. In Fig. 4 (a) and (b) we observe that the probability distribution in the direction parallel to the polarization axis extends from about 5 to 25 eV approximately, very similar to the experimental data in Fig. 1 (a) and (b). Besides, for emission perpendicular to the polarization axis, the maximum lies about 14 eV in both calculations [in Fig. 4 (a) and (b)] and measurements [in Fig. 1 (a) and (b)].

In order to recover the intracycle interference pattern, we repeat the procedure performed for the experimental data and calculate a difference map subtracting two similar intensity-averaged distributions with peak intensities of the NIR laser $I_L = 1.41 \times 10^{13}$ W/cm² and $I_L = 1.27 \times 10^{13}$ W/cm² corresponding to electric fields of $F_{L0} = 0.02$ and $F_{L0} = 0.019$, respectively. As the total measured ionization yield is unknown, we normalize the two calculated averaged electron-angle distributions before subtracting. Therefore, the difference shows positive and negative values in Fig. 4 (c) and (d) for TDSE and SFA, respectively. Even though the distribution in Fig. 4 (c) and (d) cannot be thought of as a probability distribution due to the existence of negative values, the intracycle structure pattern can be easily identified in the

figure (compare to single intensity non-intensity-averaged probability distribution in Fig. 2). There is a strong similarity between the intracycle interference pattern of Figs. 3 (a) and (b) and the difference map of Figs. 4 (c) and (d) for the respective TDSE and SFA calculations. To account for experimental resolution we have smoothed the calculations using an energy window of about 1 eV and an angle of about 5°. The intracycle interference pattern is recovered, as can be easily seen by comparing it to Figs. 2 (a) and (b). Besides, from comparing Fig. 3 (b) to (a) we can say that the SFA reproduce the TDSE quite accurately. In both the TDSE and the SFA calculations the interference structure can be retrieved with the subtraction procedure used for the treatment of the experimental data. Therefore we can state that our calculations both reproduce the experiment remarkably well.

5 Conclusions

We performed experiments on laser-assisted XUV ionization of argon atoms and recorded energy- and angle-resolved photoelectron spectra. We see that the intracycle interference pattern is smeared out and cannot be directly observed after accounted for the average over the focal volume. However, by subtracting two angle-resolved photoelectron spectra for slightly different NIR laser intensities the intracycle interference pattern is recovered. We have performed TDSE *ab initio* and SFA calculations and averaged them over the focal volume of the XUV and NIR laser pulses to compare with experiments. Both TDSE and SFA are in good agreement corresponding well to the experiment. By performing simulations using a flattop XUV pulse that comprises only one optical laser cycle, we observed a clear intracycle interference pattern very similar to the theoretically and experimentally extracted by subtracting distributions for slightly different laser intensities. We have also shown that theoretical calculations of LAPE are a useful tool to determine the elusive experimental NIR laser intensity.

We have retrieved intracycle interference fringes in electron emission produced by atomic argon ionization subject to an XUV pulse in the presence of a strong near-infrared laser pulse with both pulses linearly polarized in the same direction.

6 Acknowledgements

We are grateful to N. Kabachnik for fruitful discussions and early support. Work supported by bilateral Argentine-German grant CONICET-DAAD of 2015, the grant of Deutsche Forschungsgemeinschaft (KO 4920/1-1), and by CONICET PIP0386, PICT-2016-0296 and PICT-2014-2363 of ANPCyT (Argentina).

7 Authors contributions

J. Hummert, M. Kubin, and O. Kornilov performed the experiment, and S. D. López and D. G. Arbó performed

the theoretical calculations. All the authors were involved in the preparation of the manuscript and have read and approved the final manuscript.

References

1. J. Itatani, F. Quéré, G. L. Yudin, M. Yu. Ivanov, F. Krausz, and P. B. Corkum. Attosecond streak camera. *Phys. Rev. Lett.*, 88:173903, Apr 2002.
2. Ulrike Frühling, Marek Wieland, Michael Gensch, Thomas Gebert, Bernd Schutte, Maria Krikunova, Roland Kalms, Filip Budzyn, Oliver Grimm, Jorg Rossbach, Elke Plonjes, and Markus Drescher. Single-shot terahertz-field-driven x-ray streak camera. *Nat Photon*, 3(9):523–528, Sep 2009.
3. M. Wickenhauser, J. Burgdörfer, F. Krausz, and M. Drescher. Attosecond streaking of overlapping fano resonances. *Journal of Modern Optics*, 53(1-2):247–257, 2006.
4. S Düsterer, L Rading, P Johnsson, A Rouzée, A Hundertmark, M J J Vrakking, P Radcliffe, M Meyer, A K Kazansky, and N M Kabachnik. Interference in the angular distribution of photoelectrons in superimposed xuv and optical laser fields. *Journal of Physics B: Atomic, Molecular and Optical Physics*, 46(16):164026, 2013.
5. M. Meyer, J. T. Costello, S. Düsterer, W. B. Li, and P. Radcliffe. Two-colour experiments in the gas phase. *Journal of Physics B Atomic Molecular Physics*, 43(19):194006, October 2010.
6. M. Meyer, P. Radcliffe, T. Tschentscher, J. T. Costello, A. L. Cavalieri, I. Grguras, A. R. Maier, R. Kienberger, J. Bozek, C. Bostedt, S. Schorb, R. Coffee, M. Messerschmidt, C. Roedig, E. Sistrunk, L. F. di Mauro, G. Doumy, K. Ueda, S. Wada, S. Düsterer, A. K. Kazansky, and N. M. Kabachnik. Angle-Resolved Electron Spectroscopy of Laser-Assisted Auger Decay Induced by a Few-Femtosecond X-Ray Pulse. *Physical Review Letters*, 108(6):063007, February 2012.
7. P. Radcliffe, M. Arbeiter, W. B. Li, S. Düsterer, H. Redlin, P. Hayden, P. Hough, V. Richardson, J. T. Costello, T. Fennel, and M. Meyer. Atomic photoionization in combined intense XUV free-electron and infrared laser fields. *New Journal of Physics*, 14(4):043008, April 2012.
8. M. J. Nandor, M. A. Walker, L. D. Van Woerkom, and H. G. Muller. Detailed comparison of above-threshold-ionization spectra from accurate numerical integrations and high-resolution measurements. *Phys. Rev. A*, 60:R1771–R1774, Sep 1999.
9. H. G. Muller. Numerical simulation of high-order above-threshold-ionization enhancement in argon. *Phys. Rev. A*, 60:1341–1350, Aug 1999.
10. A K Kazansky and N M Kabachnik. On the gross structure of sidebands in the spectra of laser-assisted auger decay. *Journal of Physics B: Atomic, Molecular and Optical Physics*, 43(3):035601, 2010.
11. A. K. Kazansky, I. P. Sazhina, and N. M. Kabachnik. Angle-resolved electron spectra in short-pulse two-color xuv+ir photoionization of atoms. *Phys. Rev. A*, 82:033420, Sep 2010.
12. S. Bivona, G. Bonanno, R. Burlon, and C. Leone. Two-color ionization of hydrogen by short intense pulses. *Laser Physics*, 20(12):2036–2044, 2010.
13. J. M. Schins, P. Breger, P. Agostini, R. C. Constantinescu, H. G. Muller, G. Grillon, A. Antonetti, and A. Mysyrowicz. Observation of laser-assisted auger decay in argon. *Phys. Rev. Lett.*, 73:2180–2183, Oct 1994.
14. Diego G. Arbó, Kenichi L. Ishikawa, Klaus Schiessl, Emil Persson, and Joachim Burgdörfer. Intracycle and intercycle interferences in above-threshold ionization: The time grating. *Phys. Rev. A*, 81:021403, Feb 2010.
15. Diego G. Arbó, Kenichi L. Ishikawa, Klaus Schiessl, Emil Persson, and Joachim Burgdörfer. Diffraction at a time grating in above-threshold ionization: The influence of the coulomb potential. *Phys. Rev. A*, 82:043426, Oct 2010.
16. A. A. Gramajo, R. Della Picca, C. R. Garibotti, and D. G. Arbó. Intra- and intercycle interference of electron emissions in laser-assisted XUV atomic ionization. *Physical Review A*, 94(5):053404, November 2016.
17. A. A. Gramajo, R. Della Picca, and D. G. Arbó. Electron emission perpendicular to the polarization direction in laser-assisted XUV atomic ionization. *Physical Review A*, 96(2):023414, August 2017.
18. A. A. Gramajo, R. Della Picca, S. D. López, and D. G. Arbó. Intra- and intercycle interference of angle-resolved electron emission in laser-assisted XUV atomic ionization. *Journal of Physics B Atomic Molecular Physics*, 51(5):055603, March 2018.
19. Martin Eckstein, Chung-Hsin Yang, Markus Kubin, Fabio Frassetto, Luca Poletto, Hans-Hermann Ritze, Marc J. J. Vrakking, and Oleg Kornilov. Dynamics of n2 dissociation upon inner-valence ionization by wavelength-selected xuv pulses. *The Journal of Physical Chemistry Letters*, 6(3):419–425, 2015. PMID: 26261958.
20. A. T. J. B. Eppink and D. H. Parker. Velocity map imaging of ions and electrons using electrostatic lenses: Application in photoelectron and photofragment ion imaging of molecular oxygen. *Review of Scientific Instruments*, 68:3477–3484, September 1997.
21. Ji-Wei Geng, Liang-You Peng, Shu-Na Song, and Qihuang Gong. Interference structures in photoelectron spectra of atoms ionized by xuv pulses in the presence of a strong ir field. *Phys. Rev. A*, 88:053418, Nov 2013.
22. Markus Kubin. Wavelength-tunable xuv-pulses for femtosecond xuv-ir nonlinear effects. *Master’s Thesis, Freie Universität Berlin, Berlin*, 2013.
23. X. M. Tong and S. I. Chu. Theoretical study of multiple high-order harmonic generation by intense ultrashort pulsed laser fields: A new generalized pseudospectral time-dependent method. *Chem. Phys.*, 217(2-3):119–130, 1997.
24. Xiao-Min Tong and Shih-I Chu. Time-dependent approach to high-resolution spectroscopy and quantum dynamics of rydberg atoms in crossed magnetic and electric fields. *Phys. Rev. A*, 61:031401, Feb 2000.
25. X M Tong and C D Lin. Empirical formula for static field ionization rates of atoms and molecules by lasers in the barrier-suppression regime. *Journal of Physics B: Atomic, Molecular and Optical Physics*, 38(15):2593, 2005.
26. H. G. Muller and F. C. Kooiman. Bunching and Focusing of Tunneling Wave Packets in Enhancement of High-Order Above-Threshold Ionization. *Physical Review Letters*, 81:1207–1210, August 1998.
27. O Schöller, J S Briggs, and R M Dreizler. Coherent excitation of hydrogen atoms by proton impact. *Journal of Physics B: Atomic and Molecular Physics*, 19(16):2505, 1986.

28. A. Messiah. *Quantum mechanics i*. 1965. North-Holland, New York.
29. S. Dionissopoulou, Th. Mercouris, A. Lyras, and C. A. Nicolaides. Strong laser-field effects in hydrogen: high-order above-threshold ionization and photoelectron angular distributions. *Phys. Rev. A*, 55:4397–4406, Jun 1997.
30. P. A. Macri, J. E. Miraglia, and M. S. Gravielle. Ionization of hydrogen targets by short laser pulses. *Journal of the Optical Society of America B Optical Physics*, 20:1801–1806, September 2003.
31. D.M. Wolkow. Über eine klasse von lösungen der diracschen gleichung. *Zeitschrift für Physik*, 94(3-4):250–260, 1935.
32. J. Posthumus. *Molecules and Clusters in Intense Laser Fields*. September 2009.
33. S. Augst, D. D. Meyerhofer, D. Strickland, and S. L. Chin. Laser ionization of noble gases by Coulomb-barrier suppression. *Journal of the Optical Society of America B Optical Physics*, 8:858–867, April 1991.
34. Martin Eckstein, Johan Hummert, Markus Kubin, Chung-Hsin Yang, Fabio Frassetto, Luca Poletto, Marc JJ Vrakking, and Oleg Kornilov. Alignment and characterization of the two-stage time delay compensating XUV monochromator. *arXiv preprint arXiv:1604.02650*, 2016.